Volume 12
Number 4
28 January 2024
Pages 833–1116

Journal of Materials Chemistry B

Materials for biology and medicine

rsc.li/materials-b

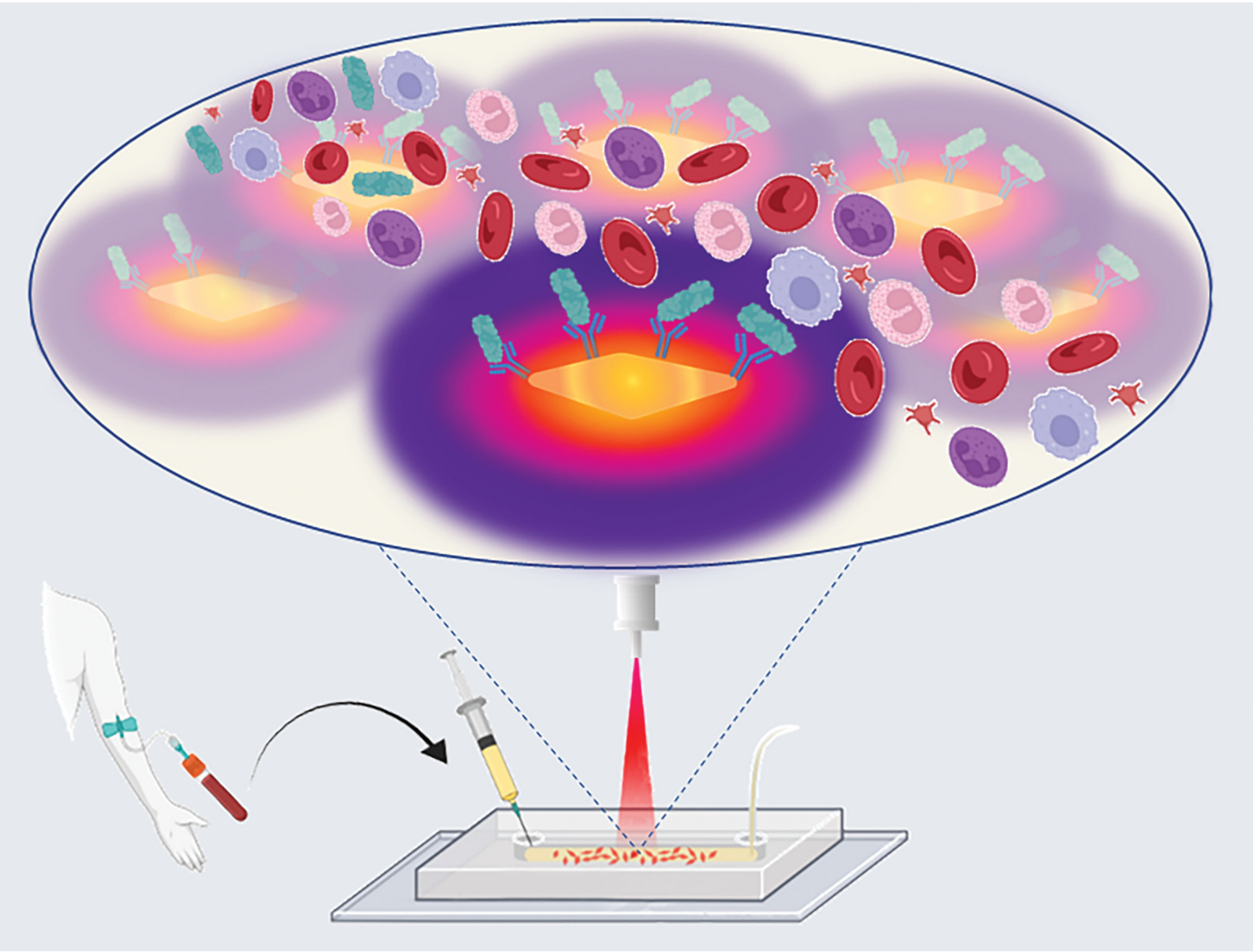

ISSN 2050-750X

ROYAL SOCIETY OF CHEMISTRY

PAPER

Monica Focsan *et al.*

Portable microfluidic plasmonic chip for fast real-time cardiac troponin I biomarker thermoplasmonic detection

Journal of Materials Chemistry B

ROYAL SOCIETY OF CHEMISTRY

PAPER

View Article Online
View Journal | View Issue

Cite this: J. Mater. Chem. B, 2024, 12, 962

Portable microfluidic plasmonic chip for fast real-time cardiac troponin I biomarker thermoplasmonic detection†

Andreea Campu,[a] Ilinca Muresan,[a] Monica Potara,[a] Diana Raluca Lazar,[bc] Florin-Leontin Lazar,[d] Simona Cainap,[be] Dan Mircea Olinic,[df] Dana Maniu,[ag] Simion Astilean[ag] and Monica Focsan[*ag]

Acute myocardial infarction is one of the most serious cardiovascular pathologies, impacting patients' long-term outcomes and health systems worldwide. Significant effort is directed toward the development of biosensing technologies, which are able to efficiently and accurately detect an early rise of cardiac troponin levels, the gold standard in detecting myocardial injury. In this context, this work aims to develop a microfluidic plasmonic chip for the fast and accurate real-time detection of the cardiac troponin I biomarker (cTnI) *via* three complementary detection techniques using portable equipment. Furthermore, the study focuses on providing a better understanding of the thermoplasmonic biosensing mechanism taking advantage of the intrinsic photothermal properties of gold nanoparticles. Specifically, a plasmonic nanoplatform based on immobilized gold nanobipyramids was fabricated, exhibiting optical and thermoplasmonic properties that promote, based on a sandwich-like immunoassay, the "proof-of-concept" multimodal detection of cTnI *via* localized surface plasmon resonance, surface enhanced Raman spectroscopy and thermoplasmonic effects under simulated conditions. Furthermore, after the integration of the plasmonic nanoplatform in a microfluidic channel, the determination of cTnI in 16 real plasma samples was successfully realized *via* thermoplasmonic detection. The results are compared with a conventional high-sensitivity enzyme-linked immunosorbent clinical assay (ELISA), showing high sensitivity (75%) and specificity (100%) as well as fast response features (5 minutes). Thus, the proposed portable and miniaturized microfluidic plasmonic chip is successfully validated for clinical applications and transferred to clinical settings for the early diagnosis of cardiac diseases, leading towards the progress of personalized medicine.

Received 19th September 2023,
Accepted 16th November 2023

DOI: 10.1039/d3tb02190d

rsc.li/materials-b

[a] Nanobiophotonics and Laser Microspectroscopy Center, Interdisciplinary Research Institute in Bio-Nano-Sciences, Babes-Bolyai University, Treboniu Laurian No. 42, 400271 Cluj-Napoca, Romania. E-mail: monica.iosin@ubbcluj.ro
[b] Department of Pediatric Cardiology, Pediatric Clinic No. 2, Emergency County Hospital for Children, Crisan No. 3 – 5, 400124 Cluj-Napoca, Romania
[c] 11th Department of Medical Oncology, University of Medicine and Pharmacology "Iuliu Hatieganu", Republicii No. 34 – 36, 400171 Cluj-Napoca, Romania
[d] Department of Interventional Cardiology, Medical Clinic No. 1, Emergency County Hospital, Clinicilor No. 3 – 5, 400006 Cluj-Napoca, Romania
[e] Department of Mother & Child, University of Medicine and Pharmacology "Iuliu Hatieganu", Louis Pasteur No. 4, 400349 Cluj-Napoca, Romania
[f] Cardiology Discipline, University of Medicine and Pharmacology "Iuliu Hatieganu", Louis Pasteur No. 4, 400349 Cluj-Napoca, Romania
[g] Biomolecular Physics Department, Faculty of Physics, Babes-Bolyai University, Mihail Kogalniceanu No. 1, 400084 Cluj-Napoca, Romania

† Electronic supplementary information (ESI) available: Materials, characterization methods, gold nanobipyramids synthesis, statistical analysis, inclusion and exclusion criteria, characteristics of the cohort, characterization of the gold nanobipyramids and plasmonic nanoplatform, thermal determinations, and clinical assay of the adult population. See DOI: https://doi.org/10.1039/d3tb02190d

Introduction

As one of the most common cardiovascular diseases, acute myocardial infarction (AMI) is recognised as the most severe cardiac ailment and was declared by the World Health Organization (WHO) as a leading cause of death[1] with an estimated 23.3 million fatalities expected by 2030.[2] The latest European Guidelines on myocardial infarction granted cardiac troponins, when assessed using high-sensitivity assays, a central role in the diagnosis algorithm.[3] As coronary artery disease is a leading cause of morbidity and mortality worldwide and its evolution can cause rapid health deterioration in patients with acute coronary syndromes, a fast and accurate diagnosis is of crucial importance in optimizing these vulnerable patients' management and improving their long-term outcomes. A conventional technique to identify AMI is electrocardiography (ECG), however a large number of patients can present a normal or non-diagnostic ECG upon their first medical contact, while 25% of the patients diagnosed with AMI are symptom-free.[4]

Since high-sensitivity cardiac troponins have emerged as the gold standard in detecting myocardial injury, the use of this biomarker allows precise diagnosis or exclusion of even small myocardial infarction in an adequate period of time, with major clinical implications: a short diagnosis-to-intervention time and a reduction of unnecessary investigations in the emergency room. The cardiac biomarkers are released from the heart into the circulation as a result of a cardiac or cardiovascular injury.[5] Cardiac troponin I (cTnI) is one of the cardiac troponin (cTn) subunits, a structural protein present in myocardial cells' contractile apparatus.[3] cTnI is an exceptionally valuable biomarker for the early detection of many life-threatening cardiac pathologies, such as coronary artery disease,[6] pulmonary embolism[7] or acute aortic dissection,[8] taking into consideration that in healthy individuals its level ranges between 1–50 ng L^{-1}.[9] Regarding patients presenting a non-ST-segment elevation myocardial infarction (NSTEMI), the accurate determination of cTnI is crucial for effective management, as it has the ability to rapidly rule-in or rule-out myocardial injury.[10,11] Conventional analytical techniques for cTnI detection are radioimmunoassay (RIA),[12] electro-generated chemiluminescence immunoassay (ECLIA)[13,14] and enzyme-linked immunosorbent assay (ELISA).[15] Sensitivity, multi-step sample processing, extended analysis times, and overall cost are the major drawbacks of these approaches. Additionally, they are unavailable in environments with limited resources because of a lack of competent staff or basic infrastructure. The ability to diagnose heart injury early is critical to the patient's prognosis. This highlights the requirement for effective, straightforward, and quick approaches for cTnI biomarker detection. In this clinical context, there is high demand for a biosensing technology able to provide fast, real-time and accurate cTnI detection to support the immediate diagnosis and informed decision-making by medical personnel.

In response to this specific demand and to overcome the major drawbacks of conventional detection methods, considerable attention has been focused on the development of Point-of-Care (PoC) devices, which present advantages such as specificity, efficiency, precision, portability, as well as ease-of-use and low costs, leading towards personalized medicine in terms of medical event prediction, appropriate treatment and improved prognosis.[16] In particular, microfluidic PoC devices are able to rapidly detect biomarkers with high efficiency due to their increased sensitivity, while considerably reducing the cost of testing – no need for well-trained operators and complex laboratory equipment, reagents and sample volume and analysis time.[17,18] The coupling of microfluidics with plasmon-based high throughput techniques such as Localized Surface Plasmon Resonance (LSPR), Surface Enhanced Raman Spectroscopy (SERS), *etc.* leads to the development of highly efficient novel PoC devices due to the versatility and high sensitivity of the plasmonic biosensor designs.[19] For the cTnI detection specifically, according to literature, SERS is much more employed in microfluidic chips compared to LSPR-based detection. Several SERS substrates were implemented to efficiently evidence the cTnI biomarker using gold nanospheres (AuNPs)[20,21] or gold nanostars[22] as SERS nanoprobes to achieve high sensitivity and, implicitly, low detection limits.[23] To our knowledge, there were only a few microfluidic devices developed for cTnI SERS detection, for example the use of plasmonic nanostrip microcone arrays has shown promising results.[24] Additionally, AuNPs coupled with magnetic beads were successfully implemented as signal transducers for LSPR detection.[25] Furthermore, the first approaches to exploit the heat generated by gold nanoparticles for biomedical applications emerged in the early 2000s,[26,27] thus becoming the foundation of the rapidly growing and promising field called thermoplasmonics.[28] Thermoplasmonics is currently implemented in applications such as photothermal therapy,[29] drug and gene delivery[30] and photoacoustic imaging,[31] despite the fact that the mechanism of nanoscale photothermal processes is still not fully understood.[32] A newly emerging application based on the intrinsic ability of gold nanoparticles to convert light-to-heat is thermoplasmonic detection. The thermal effect relies on a series of waterfall phenomena, which are dependent on the nanoparticles' material (*e.g.* mass, specific heat) and their absorption properties given by their shape and size, thus the addition of a small amount of analyte onto the surface of the nanoparticles can have a great impact on their photothermal properties. A better understanding of the thermoplasmonic effect could lead to the development of ultrasensitive biosensors, which would be able to provide a result in a matter of minutes –crucial for fast diagnosis in cases such as those of AMI, where the first hours are vital for survival. In this context, the development of a microfluidic plasmonic chip enabling the implementation of multiple analytical tools such as LSPR-SERS and thermoplasmonic detection onto the same substrate for cTnI detection is of high interest.

In this work, we aim to develop a microfluidic chip integrating a plasmonic nanoplatform for the real-time fast and on-site detection of the cardiac troponin I biomarker detection both under simulated conditions and in real sample applications. The focus in the development of the proposed chip was to overcome the limitations of conventional methods and allow unspecialized personnel to perform the test in clinical settings in order to obtain a fast, real-time and accurate response in view of early diagnosis of diseases such as AMI, where the first hours are crucial for survival. In this context, after the immobilization of the gold nanobipyramidally-shaped nanoparticles (AuBPs) onto the glass substrate, the optical properties were verified and, more interestingly, the photothermal performance of the plasmonic nanoplatform was determined, proving the preservation of the AuBPs capability to efficiently convert light-to-heat upon irradiation, thus highlighting the potential implementation for thermoplasmonic detection of biomolecules – a new and less studied detection technique. Furthermore, cTnI was successfully detected *via* LSPR, SERS and thermoplasmonic sensing under simulated conditions using a sandwich-like immunoassay standing as ''proof-of-concept'' for the multimodal detection capabilities of the plasmonic nanoplatform. After its integration in the microfluidic chip – to decrease sample volume and avoid chip and sample contamination,

the developed microfluidic plasmonic chip was validated for thermoplasmonic detection of the cTnI biomarker in 16 real plasma samples, using a portable 785 nm laser and thermographic camera, and the obtained results were in good agreement with the clinical ELISA determinations, indicating a sensitivity of 75% and 100% specificity. The design's portability and miniaturization, not only in terms of the chip but also equipment size, as well as rapid response (result in 5 minutes) allowed its implementation for the fast-on-site detection of cTnI in clinical settings without major infrastructure and unspecialized personnel to aid in the early diagnosis of various cardiac diseases.

Experimental section

The materials, characterization methods, gold nanobipyramids synthesis and statistical analysis data are presented in the ESI.†

Fabrication of the plasmonic nanoplatforms

In order to produce the plasmonic nanoplatforms, an adapted version of a previously developed AuBP self-assembly protocol was used.[33] Briefly, the commercially available glass substrates underwent a thorough cleaning process through successive rounds of 15 minute sonication in alkaline detergent, ultrapure water, acetone, and ethanol. Furthermore, the glass substrates were dried for 10 minutes at 90 °C and ozone treated at 25 °C for 5 minutes using a PSD Pro Series UV Ozone System. To ensure immobilization of the AuBPs, the clean glass substrates underwent a silanization process by immersion in 1% APTES ethanolic solution overnight at room temperature, and the samples were kept in the dark. The APTES excess was removed by rinsing the substrates with ethanol. Then, 200 μl of the colloidal AuBPs were dropped on the APTES-functionalized substrate and left overnight to self-assemble onto the substrate's surface. Further, the AuBPs-immobilized glass substrate is noted/denoted as plasmonic nanoplatform.

Fabrication of the microfluidic channels and assembly of the final plasmonic microfluidic chip

The next step in the development of the final microfluidic device was the fabrication of the microfluidic channels. Specifically, by employing a Sylgard 182 elastomer kit, polydimethylsiloxane sheets were obtained by mixing the PDMS precursor with the corresponding curing agent in a 10 : 1 weight ratio followed by the removal of the air bubbles using a vacuum desiccator for 30 minutes and pouring equal amounts (~1.4 g) of the mixture into plastic molds, which were then thermally treated at 65 °C for 1 hour.[33,34] After hardening, the PDMS was extracted from the molds and, using an Epilog Zinc 16 Laser Cutter, different microfluidic channel models were engraved into the PDMS (Fig. S1, ESI†). The models were designed and scaled as desired using the graphic design software Corel. The proposed fabrication method allows the design of microfluidic channels to suit the desired application. For further use in detection applications, shape 1 in Fig. S1 (ESI†) of the

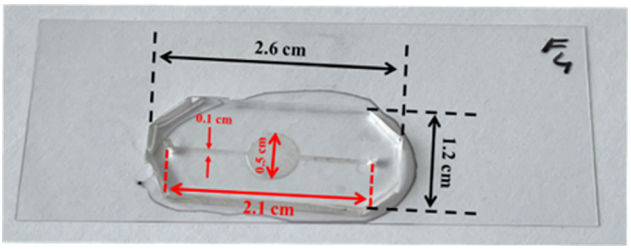

Fig. 1 The as-developed final microfluidic plasmonic chip.

microfluidic channels was selected for the assembly of the final microfluidic chip, since it ensures a bigger detection area comprised in the circle. The dimensions of the PDMS are 2.6 × 1.2 cm length × width, the microfluidic channel is 2.1 cm long × 0.1 cm wide and the detection area has a diameter of 0.5 cm. Prior to the assembly, the inlet and outlet were drilled using a 1.2 mm Rapid-Core Microfluidic Puncher to allow the insertion of the injection and withdrawal connector tubes.

To assemble the final microfluidic chip, both the plasmonic nanoplatform and PDMS microfluidic channel were plasma treated for 40 seconds using the low-pressure plasma system TETRA 30 PC/PCCE working at a 0.2 mbar pressure and 60 W power (20% of the maximum 300 W of the 13.56 MHz radio frequency generator). Afterwards, the two components were immediately brought into contact to form a permanent bond, thus obtaining the final portable microfluidic plasmonic chip (Fig. 1). Finally, the connector tubes were inserted in the inlet and outlet, and, to provide a continuous reagent and sample flow, these were further connected to an automated syringe pump system (NE-4000 Programable Syringe from NEW ERA, Pump systems Inc.).

Biosensing protocol

To evaluate the plasmonic nanoplatform's capabilities to detect the cTnI biomarker, the following sandwich assay (Scheme 1) was developed and employed: the plasmonic nanoplatform was successively functionalized with 20 μL of p-ATP 10^{-3} M (in ethanol), GA 5% as the linker molecule for protein bonding, the antibody anti-troponin 5 μg mL^{-1} (anti-cTnI) and, lastly, the biomarker troponin 3.5 μg mL^{-1} (cTnI). After every addition,

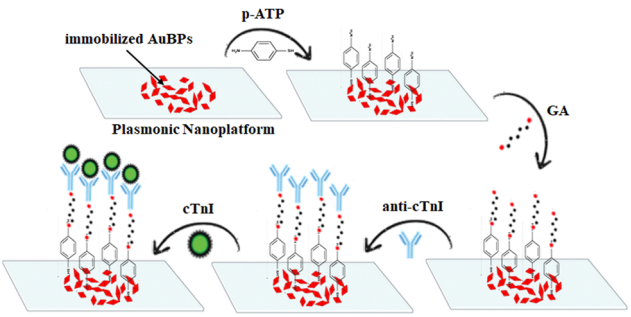

Scheme 1 Schematic illustration of the developed biosensing protocol for the cTnI biomarker detection.

the incubation time was 1 hour at room temperature. For the calibration curve, cTnI concentrations ranging from 3.5 μg mL^{-1} to 10 pg mL^{-1} were used. The same biosensing protocol was employed for the validation of the final microfluidic plasmonic chip as an efficient LSPR biosensor for clinical real-sample applications. After the successive injection and retrieval of p-ATP, GA and anti-cTnI, plasma from pediatric patients was introduced in the microfluidic plasmonic chip for real-sample analysis.

Clinical cTnI samples and assay

In this study, a total of 80 blood samples obtained between 01 February and 30 September 2020 were analyzed, of which 50 blood samples were collected from adult patients admitted to the Emergency County Hospital Cluj-Napoca, Medical Clinic No. 1, Department of Interventional Cardiology No. 2 and 30 blood samples were obtained from a pediatric population admitted to the Emergency County Hospital for Children, Pediatric Clinic No. 2, Department of Pediatric Cardiology, Cluj-Napoca. Prior to the sample collection, each patient/legal guardian of the patient (for pediatric patients) signed an informed consent form, expressing their agreement for the collected biological samples to be used for scientific purposes. The inclusion and exclusion criteria for both adult and pediatric patients are listed in the ESI† along with the main characteristics of the cohort depicted in Table S1 and Fig. S2 (ESI†). A 5 mL blood sample was collected from every patient included in the current study. All samples were centrifuged at high-speed, and part of the obtained plasma was used for troponin detection and the rest of the cell-free supernatant was stored at −20 °C. The blood samples collected at night or early in the morning were considered inappropriate, due to circadian variability.

For the cardiac troponin I detection, all samples were analyzed using the ADVIA Centaur Immunoassay XPT system from Siemens Healthcare GmbH (Erlangen, Germany). This system uses a 5th generation 3-site sandwich immunoassay, using direct chemiluminometric technology, which can detect cardiac troponins with very high sensitivity. The ELISA immunoassay consists of 3 different phases. In the first phase, the antibodies are directed against the unique N-terminal amino acid sequences. The basis of this immunological phase is represented by the particular structure of the cardiac troponin, which presents 31 specific amino acid residues on its N-terminal, allowing specific monoclonal antibody development,[35] and Solid Phase reagent used by the ADVIA Centaur TNIH, which is represented by magnetic latex particles conjugated with streptavidin with two bound biotinylated capture monoclonal antibodies, each recognizing a unique cTnI epitope. The second phase consists of another antibody-antigen reaction, in which the Lite Reagent used by the ADVIA Centaur TNIH is of great importance. The reagent comprises a conjugate, whose architecture consists of a proprietary acridinium ester and recombinant anti-human cTnI sheep Fab covalently attached to bovine serum albumin (BSA) for chemiluminescent detection, which represents the final phase. A direct relationship exists between the amount of cTnI present in the patient sample and amount of relative light units (RLUs) detected by the system, thus making quantification possible. This method has a limit of detection (LOD) of 1.6 ng L^{-1} and limit of quantification (LOQ) of 2.5 ng L^{-1}, with 20–30 minutes required for testing. The high sensitivity of the test is also augmented by its limit of blank (LOB) of 0.90 pg mL^{-1} (ng L^{-1}), which represents the highest measurement result that is likely to be observed for a blank sample.

Results and discussion

Thermoplasmonic characterization of the plasmonic nanoplatform

As the next step after the immobilization of the AuBPs onto the glass substrates, the optical and morphological properties of the as-developed plasmonic nanoplatform were determined and are presented in the ESI.†

In more recent years, a new detection tool was developed, specifically for thermoplasmonic detection. Moreover, our group has demonstrated that AuBPs possess the intrinsic ability to efficiently convert light-to-heat, thus performing as effective thermoplasmonic generators.[36] In this context, we addressed the photothermal properties of the obtained plasmonic nanoplatform by exposing it to the 785 nm laser line at a laser power density of 2.59 W cm^{-2} for 60 seconds, after which the laser was turned off and the cooling process was monitored for another 60 seconds. The experimental setup was realized to enable the sample irradiation for above, while the thermographic camera was aligned at a 45° angle with respect to the laser (Fig. S5(a), ESI†). To avoid any thermal interference or external contributions, the plasmonic substrate was suspended in air. From the analysis of the thermographic images (Fig. S5(b), ESI†) recorded every second during the irradiation and cooling process, the reached temperature (T) was extracted and the temperature difference (ΔT) was calculated with respect to the ambient temperature (T_{amb}) and plotted against the exposure time (Fig. 2(a)). A 4 °C increase in T was observed, proving that, along with the optical and electromagnetic properties, the AuBPs also preserved their intrinsic thermoplasmonic features after their immobilization onto the glass substrate. The glass substrate does not exhibit any temperature increase (Fig. 2(a) – black spectrum). Furthermore, the laser power density was increased leading to an increasing ΔT up to 19 °C for a laser power density of 7.16 W cm^{-2}. The plot of ΔT against the laser power density (Fig. S6(a), ESI†) indicated linear dependence between the increase of ΔT as a consequence of rising laser power density. The steady-state T was reached after 16 seconds, while around 20 seconds are needed to return to T_{amb} after the laser was turned off, thus, for the detection of cTnI in simulated conditions, the samples were exposed for 30 seconds to the laser line. To test the thermal stability and reusability, the plasmonic nanoplatform was exposed to 5 ON – OFF laser cycles. The thermal curves (Fig. S6(b), ESI†) show that the photothermal performances are maintained, proving the thermal stability of the as-developed plasmonic nanoplatform. The

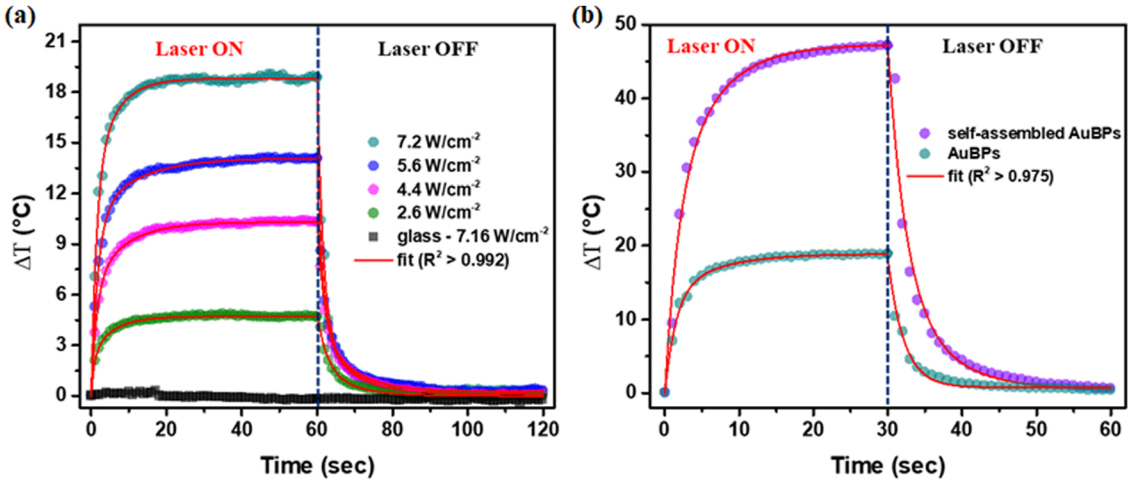

Fig. 2 (a) The heating and cooling curves resulting from the temperatures extracted from the recorded thermographic images for different laser powers. (b) The heating and cooling curves of immobilized AuBPs with lower and higher numbers of self-assemblies.

temperature differences after each cycle are considered neglectable (around 1–2%). To support these results, the LSPR response of the plasmonic substrate was monitored before and after exposure to the 785 nm laser line (Fig. S7, ESI†). No significant modifications of the optical properties of the plasmonic substrate are noticeable, indicating no laser-induced change in the morphology of the immobilized AuBPs. Thus, further implementation of the plasmonic nanoplatform for thermoplasmonic detection applications is endorsed. For further experiments, the laser power was set at 7.16 W cm^{-2} and the exposure time was decreased to 30 seconds.

To further investigate the thermoplasmonic behaviour, plasmonic nanoplatforms were fabricated to exhibit a higher number of self-assemblies by doubling the AuBPs concentration before their deposition onto the glass substrate. Fig. S8 (ESI†) depicts the normalized extinction spectra of the plasmonic nanoplatform exhibiting a lower and higher number of self-assemblies, through monitoring of the broadening of the LSPR band and a considerable red-shift, as well as the appearance of a band shoulder at higher wavelengths, which is associated with a higher amount of AuBPs self-assemblies. The plasmonic nanoplatforms were then compared in terms of photothermal conversion performance (Fig. 2(b)). By increasing the number of self-assembled AuBPs, the electromagnetic field in the interparticle gaps is strongly amplified generating the so-called extrinsic hot-spots, which considerably enhance the photothermal conversion performance. The recorded ΔT for the plasmonic nanoplatform with a higher number of self-assemblies is 2.6 times higher than for the plasmonic nanoplatform exhibiting a higher number of individual nanoparticles. The higher temperature supports a much higher detection sensitivity, hence ΔT related to the mass effect is assumed to be more evident at higher temperatures, thus its implementation for photothermal detection is also supported. Ultimately, the photothermal behaviour was investigated without and with the PDMS microfluidic channel to assess its influence onto the light-to-heat conversion performance of the self-assembled AuBPs nanoplatform. The integration of the plasmonic nanoplatform into the PDMS microfluidic device accounts for a slower heating and cooling process, however, in 30 seconds, ΔT is only 4 °C lower when the microfluidic channel is attached to the substrate, thus the thermoplasmonic effect is not considerably influenced. For the next thermoplasmonic experiments, the plasmonic nanoplatform with a higher number of self-assemblies was employed.

Evaluation of the cTnI LSPR – SERS – thermoplasmonic detection capabilities of the plasmonic nanoplatform under laboratory conditions

Furthermore, the plasmonic nanoplatform was evaluated to determine the capabilities to efficiently detect cTnI under simulated conditions *via* LSPR – SERS – thermoplasmonic sensing. The proposed biosensing protocol implies grafting of the p-ATP Raman reporter onto the surface of the immobilized AuBPs through its thiol functional group *via* back π-bonding,[37] while the remaining amino ($-NH_2$) was used to bind GA, a well-known protein cross-linking molecule with a high affinity for $-NH_2$ functional groups.[38] GA then binds the anti-cTnI antibody, which ultimately specifically captures the target cTnI biomarker. Firstly, the LSPR detection performances were evaluated by monitoring the extinction spectrum, specifically the longitudinal LSPR response, after each functionalization step (Fig. 3(a)). Thus, the covalent binding of p-ATP induces a 24 nm red-shift of the longitudinal LSPR band. The attachment of anti-cTnI *via* the GA linker leads to an additional 6 nm red-shift, while the successful capture of cTnI by the recognition element is evidenced by a 25 nm red-shift after 1 h incubation with a 3.5 μg mL^{-1} cTnI cardiac biomarker. The successive translations of the longitudinal LSPR response to higher wavelengths induced by the consecutive refractive index changes in the close vicinity of the AuBPs confirm the effective LSPR detection of cTnI under simulated conditions.

To specifically identify the cTnI biomarker captured by the recognition element, the SERS technique was employed due to

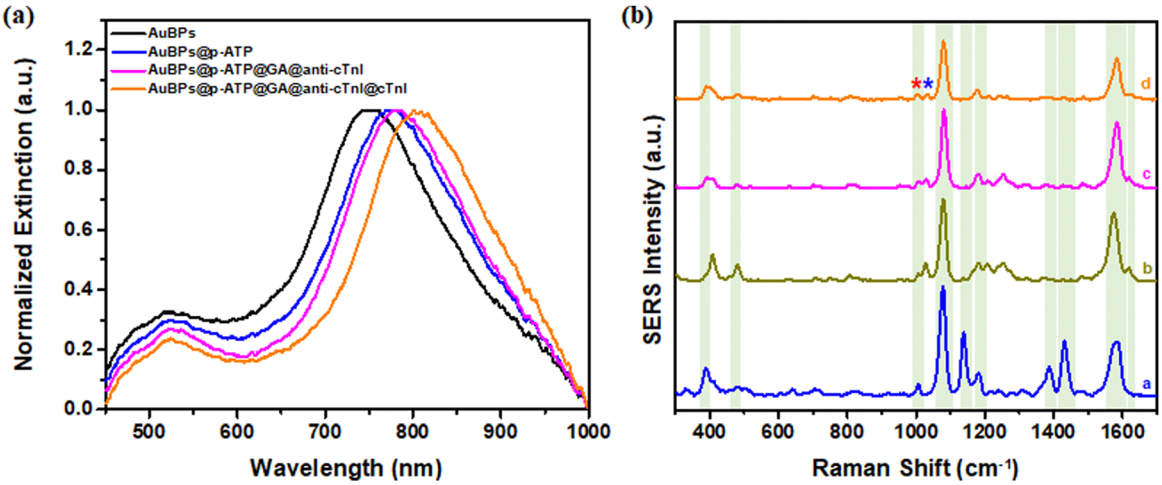

Fig. 3 (a) Extinction spectra recorded after each step of the biosensing protocol along with (b) the corresponding SERS spectra acquired with the 785 nm laser line as follows: spectrum a – after the grafting of the p-ATP, spectrum b – after the passivation with GA for non-specific binding, spectrum c – after the functionalization with the anti-cTnI antibody and spectrum d – after the successful capture of the cTnI biomarker. The characteristic p-ATP vibrational bands are marked with a light green background. The band located at 1004 cm^{-1} is marked with *, while the vibrational band at 1030 cm^{-1} is marked with *.

its capacity to deliver the distinctive vibrational fingerprint of each molecule involved in the immunological reaction. Furthermore, considering that, during the immobilization process, AuBP self-assemblies were formed and, implicitly, extrinsic "hot-spots" were generated in the interparticle nanogaps, the SERS signal is considerably enhanced,[19] thus the configuration of the proposed plasmonic nanoplatform strongly supports the implementation of the SERS detection technique. Using the 785 nm laser line, 10 SERS spectra from 10 different spots onto the plasmonic nanoplatform were recorded after each functionalization step of the biosensing protocol. Fig. 3(b) presents the obtained resulting average SERS spectra. Following the successful grafting of the p-ATP onto the AuBPs surface, the p-ATP characteristic vibrational bands (marked with a light green background) can be identified at 391 (S–C stretching, N–H_2 wagging and phenyl ring in plane deformation), 482 (N–H_2 wagging and C–H out of plane deformation), 1004 (C–C bending in phenyl ring and S–C stretching), 1073 (C–S stretching), 1141 (C–H bending and N–H_2 rocking), 1173 (C–H bending from phenyl ring), 1393 (phenyl ring deformation and N–H_2 rocking), 1437 (phenyl ring deformation and C–N stretching), 1575 (C–C stretching in phenyl ring and N–H_2 bending) and 1621 cm^{-1} (N–H_2 bending)[39] in the SERS spectrum (Fig. 3(b) – spectrum a). After the grafting of GA, the band located at 482 cm^{-1} is amplified, while the bands at 1141 and 1393 cm^{-1} assigned to the amino group vibrations are absent in the SERS spectrum, confirming the successful binding of the cross-linker molecule (Fig. 3(b) – spectrum b). The functionalization with anti-cTnI is indicated by the intensity decrease of the p-ATP characteristic vibrational bands located at 391, 482 and 1621 cm^{-1} (Fig. 3(b) – spectrum c). The successful capture of the cTnI biomarker is demonstrated by the changes of the 1004 (marked with *) and 1030 cm^{-1} (marked with *) bands ratio – the latter significantly decreasing in intensity once the cTnI biomarker is specifically captured by the corresponding antibody (Fig. 3(b) – spectrum d). Thus, the implementation of SERS allows both the detection and specific identification of the antigen – antibody interaction, confirming the LSPR determinations and demonstrating the capability of the proposed plasmonic nanoplatform to be efficiently employed in the development of diagnostic tools for clinical applications of cardiac cTnI biomarker detection leading towards accurate and fast diagnostics.

Taking advantage of the preserved AuBPs' thermoplasmonic properties, we took one step forward and tested the potential capability of the plasmonic nanoplatform to evidence the immunological reaction *via* thermoplasmonic detection. The indirect detection of the recognition interaction is realized by monitoring the changes in ΔT upon each step of the sandwich assay. In this context, the plasmonic nanoplatform was exposed to the NIR 785 nm laser line (7.16 W cm^{-2}) for 30 seconds, while thermal images were recorded every second. The plot of the extracted ΔT from the thermographic images as a function of the exposure time are represented in Fig. 4. After the grafting of the p-ATP Raman reporter, the ΔT calculated after 30 seconds irradiation decreases with 7 °C, leading to the assumption that the attachment of the p-ATP molecules onto the surface of the AuBPs has influenced their capability to convert light-to-heat under identical irradiation conditions. Additionally, a slight change in the rise of the temperature is noticed as observed in the thermal curves, implying a modification of the photothermal efficiency. The photothermal effect occurs as a result of a series of waterfall-phenomena induced by the photoexcitation of the electron cloud localized at the surface of the nanoparticles.[40,41] Thus, the modification of the photothermal conversion upon functionalization could be explained by the change in the refractive index in the vicinity of the nanoparticles.[42] The binding of GA increases the temperature by around 2 °C, while the anti-cTnI does not

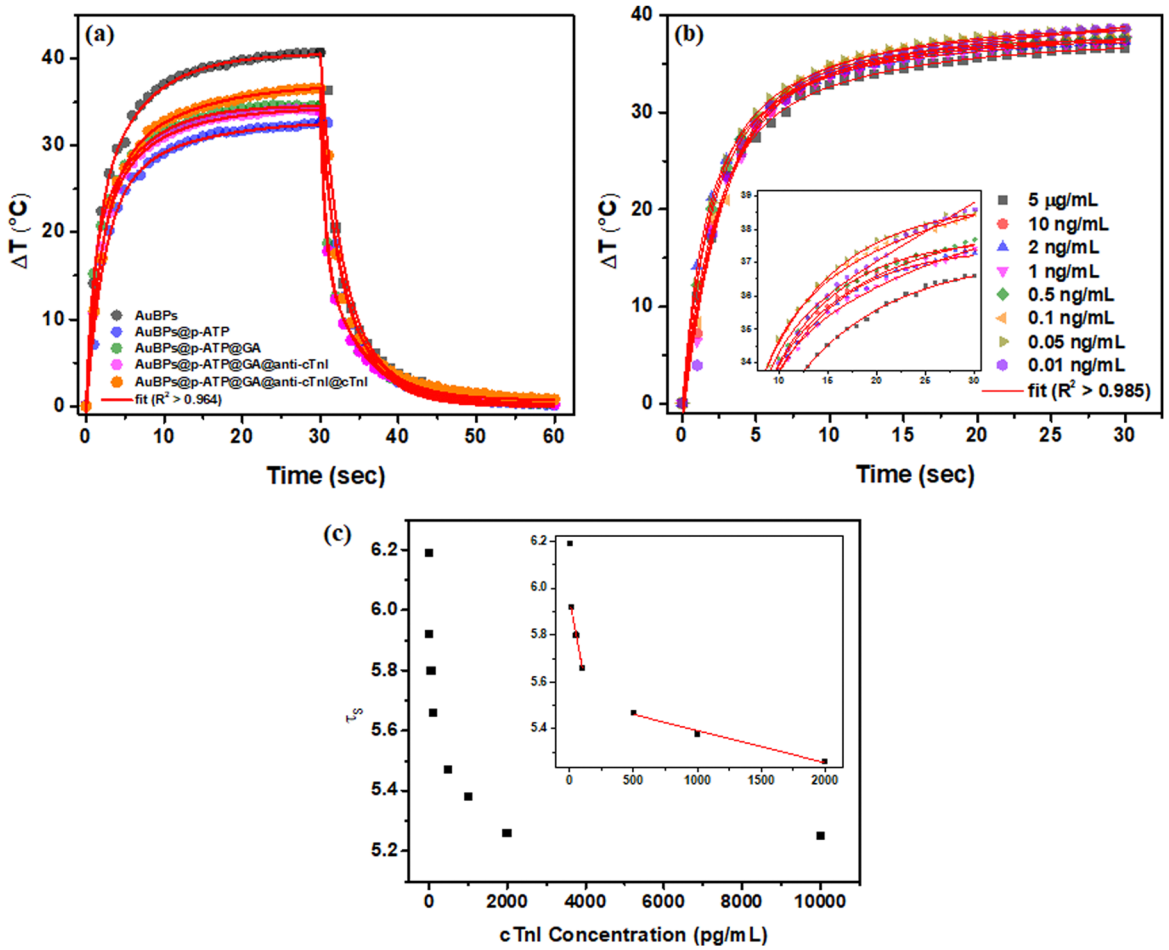

Fig. 4 (a) Thermal curves obtained after each functionalization step as well as after the specific capture of the cTnI biomarker extracted from the collected thermographic images. (b) Thermal curves obtained from the thermographic images collected after the exposure of the functionalized plasmonic nanoplatform to different concentrations of cTnI spanning from 5 μg mL^{-1} to 10 pg mL^{-1}. Inset: Zoom in on the thermal curves for better visualization. (c) Plot of cTnI concentration against τ_S. Inset: Zoom in on the 0–2000 pg mL^{-1} range of the plot for better identification of the linear ranges.

significantly alter the thermal behavior of the plasmonic nanoplatform. However, once the target cTnI biomarker is captured, the photothermal conversion of light-to-heat by the immobilized AuBPs is increased by an additional 3 °C after the 30 seconds of 785 nm laser exposure. The temperature determinations were realized in duplicate showing errors in temperature variation of approximately 1 °C for the plasmonic nanoplatform, 2 °C after the functionalization with p-ATP and GA, respectively, 1 °C after the grafting of the recognition element and 1 °C after the capture of the cTnI biomarker.

An indicator of the modification of the photothermal performance (η) is represented by the time constant τ_S of the cooling process (see the ESI†). The successive functionalization with the linkers and biorecognition molecules as well as capture of the cTnI biomarker subsequently modifies $\sum m_i C_{p,i}$ and, implicitly, τ_S. In this context, after each step of the functionalization, τ_S was determined. After the functionalization with p-ATP, τ_S rises from 4.10 (for the bare plasmonic nanoplatform) to 5.05 and increases to 6.15 after GA is grafted onto the surface of the p-ATP functionalized plasmonic nanoplatform. The addition of the anti-cTnI biorecognition molecule does not significantly modify τ_S, while the capture of the cTnI biomarker (concentration of 5 μg mL^{-1}) is evidenced by a τ_S of 4.54. These determinations lead to the assumption that the grafting of the p-ATP changes the intrinsic heat transfer rate of the oscillating electrons localized at the surface of the immobilized nanoparticles, while the binding of the biorecognition molecules and target cTnI biomarker result in an addition of substance, thus τ_S decreases due to a mass effect. The obtained results demonstrate the capability of the plasmonic nanoplatform to operate as an efficient thermoplasmonic biosensor for the detection of target biomarkers.

Furthermore, we exposed the plasmonic nanoplatform to different concentrations of cTnI spanning from 10 ng mL^{-1} to 10 pg mL^{-1}, which are relevant for the detection of cTnI. We performed the same photothermal experiments under identical conditions and based on the thermographic images we have presented the thermal curves in Fig. 4(b). As the concentration of cTnI lowers, ΔT slightly increases from 36 °C for 5 μg mL^{-1} to almost 39 °C for 10 pg mL^{-1}. In terms of τ_S, with the decrease of

the cTnI concentration τ_S increases up to the value assigned to the functionalization step with anti-cTnI, prior to the capture of the cardiac biomarker (Fig. 4(c)). In the plot of the cTnI concentration against τ_S, two linear ranges can be identified: one between 10–100 pg mL^{-1}, for which a LOD of 4.2 pg mL^{-1} and LOQ of 12.7 pg mL^{-1} were calculated, and another at higher concentrations (0.5–2 ng mL^{-1}) with a LOD of 0.47 ng mL^{-1} and LOQ of 1.43 ng mL^{-1}. The LOB was determined to be 0.94 pg mL^{-1}. The LOB, LOD and LOQ were determined using eqn (S7)–(S9) (ESI†) presented in the ESI† along with the obtained computational data. Thus, the as-developed plasmonic nanoplatform proves to be effective for cTnI detection in relevant clinical ranges of concentrations.

Clinical assay and validation of the as-designed portable microfluidic plasmonic chip for the thermoplasmonic detection of cTnI in real samples

One of the most important clinical applications of the cardiac troponin assays is represented by their vital role in the diagnosis of myocardial infarction, as, according to the Fourth universal definition of myocardial infarction, a rise and/or fall in cTn values with at least one value above the 99th percentile upper reference limit (URL) is required in order to establish the diagnosis.[3] What is more, the use of current generation high sensitivity assays led to the development of more rapid 'rule-in' and 'rule-out' MI algorithms and a shorter time from symptoms onset to diagnosis, which is of great importance for optimal management and long-term outcomes.[43] In this context, prior to the validation of the microfluidic chip for real applications, blood samples were collected and conventional ELISA cTnI biomarker testing was realized in clinical settings. For this study, both adult and pediatric patients were selected. The clinical assay regarding the adult population is discussed in the ESI.† Regarding the pediatric population, all samples were collected from patients with multisystemic inflammatory syndrome after COVID-19 infection, the average value of troponin level being 590.35 ± 368.18 pg mL^{-1}. The average age of the patients was 8.62 ± 2.11 years, well correlated with the values of inflammatory markers. Among the pediatric patients, 4 girls and 2 boys had very high troponin values (between 2000 and 3500 pg mL^{-1}), values correlated with particularly serious symptoms of multisystemic inflammatory syndrome after COVID-19 infection (Fig. S9, ESI†). Excluding these 6 extreme values, the average troponin level for pediatric patients is illustrated in Table S2 (ESI†). Only two of the pediatric patients had troponin levels within normal limits (<11 pg mL^{-1} for girls aged between 1 and 19 years, <14 pg mL^{-1} for boys aged between 1 and 19 years, and <21 pg mL^{-1} for children aged between 6 months and 1 year). Even though the prognostic value of cardiac troponins in pediatric populations has not been as well documented as in adults, and taking into consideration that hs-cTnI levels can be elevated up to 13.1% in healthy children, several studies demonstrated their role in predicting subclinical cardiomyocyte damage.[44] COVID-19 infection and its mid- and long-term effects are nowadays one of the most frequent causes of troponin elevation in children and it has been shown that early assessment of elevated hs-cTn could predict a 2-fold increase in the risk of major complications,[45] including multisystem inflammatory syndrome in children (MIS-C). Moreover, in patients with MIS-C, troponin values are usually elevated, suggesting that cardiac involvement in MIS-C patients is almost the rule.[46] However, in our study, in which all included pediatric patients were diagnosed with MIS-C, as well as in the literature, the high troponin values were not correlated with a poorer prognosis, as all patients' clinical course was satisfactory.

For validation of the microfluidic plasmonic chip for the detection of cTnI from real samples, the microfluidic channel was attached to the plasmonic nanoplatform to form the final microfluidic device (Fig. 1), thus the immunological reaction is realized in a controlled environment and the real sample volume, which is injected through the microfluidic channel, is considerably decreased. The clinical validation of the proposed microfluidic plasmonic chip was realized *via* thermoplasmonic detection, which provides the advantages of portable equipment (thermographic IR camera and laser), fast response (time needed for irradiation is 1 minute) and simple analysis of the result compared to the other techniques, thus being highly adapted for Point-of-Care applications. Next, 16 randomly selected blood samples collected by our medical collaborators from the pediatric patients were analyzed. A microfluidic chip was fabricated for each plasma sample. Before and after the injection of the plasma as received from the medical personnel in the microfluidic channel and an incubation time of 5 minutes, the microfluidic chips were exposed for 30 seconds to a 785 nm laser line, while thermographic images were recorded every second throughout the irradiation as well as for 30 seconds after the laser exposure. The temperatures were extracted from the thermographic images and τ_S was determined for each sample both before and after the cTnI capture for comparison. Out of the 16 samples, 12 samples followed the same behaviour as those under simulated conditions. τ_S decreased after the capture of the cardiac biomarker. Whereas 4 samples can be regarded as inconclusive due to a rise in τ_S with respect to the τ_S prior the plasma injection. Out of the 12 remaining samples, 11 tested positive by showing a decrease of τ_S after the capture of the cTnI biomarker, while 1 tested negative – τ_S did not change after the injection of the plasma suggesting that the sample does not contain cTnI in detectable concentrations. Fig. 5 shows the correspondence between $\Delta\tau_S$ obtained under simulated conditions and for the real samples with respect to the cTnI concentration determined by ELISA. For higher cTnI concentrations in real plasma samples, $\Delta\tau_S$ does not correlate with the one determined under laboratory conditions, however at smaller cTnI concentrations $\Delta\tau_S$ correlates well with some variations.

Additionally, the quality of the thermoplasmonic detection of the microfluidic device was assessed in comparison with the clinical ELISA cTnI values through determination of its sensitivity (S_e), specificity (S_p), positive predictive value (PPV) and negative predictive value (NPV), which are metrics that describe the adequacy of the test for clinical applications.[47] Following

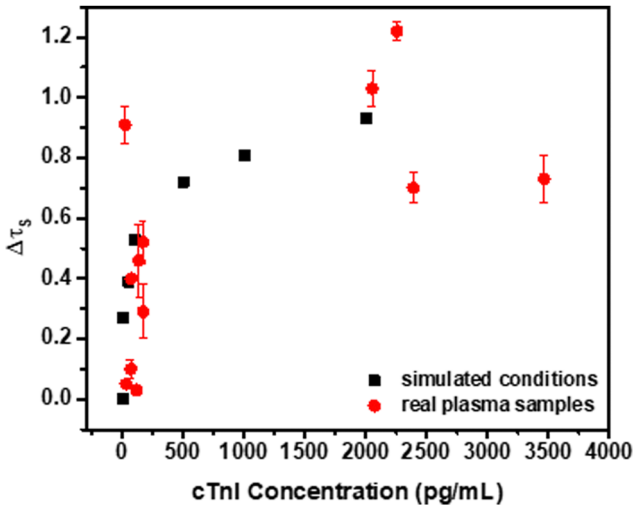

Fig. 5 Plot of the $\Delta\tau_S$ obtained under simulated conditions for the selected concentrations and $\Delta\tau_S$ obtained for the cTnI levels determined by ELISA.

eqn (S1)–(S4) (ESI†), we determined a S_e of 75% and S_p of 100%. Furthermore, implementation of the microfluidic chip was proven to be effective in the diagnosis of cardiac injuries, showing a probability of 100% for a positive test to indicate a patient suffering from a medical condition, while there is only a 25% NPV. Thus, the proposed microfluidic plasmonic chip was successfully transferred to clinical applications and demonstrated to exhibit high sensitivity and specificity as well as probability to accurately diagnose cardiac injuries.

Conclusion

To summarize, in this work, we have developed a microfluidic plasmonic chip for specific and accurate cTnI cardiac biomarker detection showing great promise for clinical fast on-site implementation due to its portability and miniaturization. The core of the microfluidic device is represented by the AuBP-based plasmonic nanoplatform, which was demonstrated to be able to operate as a multimodal LSPR–SERS–thermoplasmonic cTnI detection nanoplatform by exploiting the unique properties of the immobilized AuBPs, specifically the LSPR and strongly enhanced electromagnetic field at their tips as well as the generated extrinsic "hot-spots" formed in the interparticle gaps. Furthermore, the microfluidic plasmonic chip's thermoplasmonic detection abilities were validated for the detection of cTnI in 16 real samples, being in good agreement with the clinical determinations using hs-cTn ELISA assay. The implementation of a portable thermographic IR camera allows on-site cTnI LSPR detection with decreased analysis and response time, and the result of the test is obtained in less than 5 minutes. Thus, the developed microfluidic device is able to determine the cTnI presence quickly and accurately with a sensitivity of 75% and specificity of 100%, leading towards rapid diagnosis and treatment. The design was effectively transferred to clinical applications, strongly supporting its operation by unspecialized medical personnel and significantly contributing to the progress of cTnI biosensors and, implicitly, personalized medicine.

Conflicts of interest

The authors declare no conflict of interest.

Acknowledgements

This work was supported by CNCS-UEFISCDI Romania, under project number PN-III-P2-2.1-PED-2019-3345.

References

1 X. Han, S. Li, Z. Peng, A. M. Othman and R. Leblanc, Recent Development of Cardiac Troponin I Detection, *ACS Sens.*, 2016, **1**(2), 106–114, DOI: **10.1021/acssensors.5b00318**.
2 WHO, Global status report on noncommunicable diseases 2010, WHO.
3 K. Thygesen, J. S. Alpert, A. S. Jaffe, B. R. Chaitman, J. J. Bax, D. A. Morrow, H. D. White, ESC Scientific Document Group, K. Thygesen and J. S. Alpert, *et al.*, Fourth Universal Definition of Myocardial Infarction (2018), *Eur. Heart J.*, 2019, **40**(3), 237–269, DOI: **10.1093/eurheartj/ehy462**.
4 P. Singh, S. K. Pandey, J. Singh, S. Srivastava, S. Sachan and S. K. Singh, Biomedical Perspective of Electrochemical Nanobiosensor, *Nano-Micro Lett.*, 2016, **8**(3), 193–203, DOI: **10.1007/s40820-015-0077-x**.
5 K. Ananthan and A. R. Lyon, The Role of Biomarkers in Cardio-Oncology, *J Cardiovasc. Transl. Res.*, 2020, **13**(3), 431–450, DOI: **10.1007/s12265-020-10042-3**.
6 M. Liu, R. Jiang, M. Zheng, M. Li, Q. Yu, H. Zhu, H. Guo and H. Sun, A Sensitive Ratiometric Biosensor for Determination Cardiac Troponin I of Myocardial Infarction Markers Based on N, Zn-GQDs, *Talanta*, 2022, **249**, 123577, DOI: **10.1016/j.talanta.2022.123577**.
7 S. V. Konstantinides, G. Meyer, C. Becattini, H. Bueno, G.-J. Geersing, V.-P. Harjola, M. V. Huisman, M. Humbert, C. S. Jennings and D. Jiménez, *et al.*, 2019 ESC Guidelines for the Diagnosis and Management of Acute Pulmonary Embolism Developed in Collaboration with the European Respiratory Society (ERS, *Eur. Heart J.*, 2020, **41**(4), 543–603, DOI: **10.1093/eurheartj/ehz405**.
8 A. Forrer, F. Schoenrath, M. Torzewski, J. Schmid, U. F. W. Franke, N. Göbel, D. Aujesky, C. M. Matter, T. F. Lüscher, F. Mach, D. Nanchen, N. Rodondi, V. Falk, A. von Eckardstein and J. Gawinecka, Novel Blood Biomarkers for a Diagnostic Workup of Acute Aortic Dissection, *Diagnostics*, 2021, **11**(4), 615, DOI: **10.3390/diagnostics11040615**.
9 F. S. Apple, R. Ler and M. M. Murakami, Determination of 19 Cardiac Troponin I and T Assay 99th Percentile Values from a Common Presumably Healthy Population, *Clin.*

Chem., 2012, **58**(11), 1574–1581, DOI: **10.1373/clinchem.2012.192716**.

10 T.-H. Lee, L.-C. Chen, E. Wang, C.-C. Wang, Y.-R. Lin and W.-L. Chen, Development of an Electrochemical Immunosensor for Detection of Cardiac Troponin I at the Point-of-Care, *Biosensors*, 2021, **11**(7), 210, DOI: **10.3390/bios11070210**.

11 H. Basit, A. Malik and M. R. Huecker, *Non ST Segment Elevation Myocardial Infarction, StatPearls*, StatPearls Publishing, Treasure Island (FL), 2022.

12 H. D. White, Pathobiology of Troponin Elevations, *J. Am. Coll. Cardiol.*, 2011, **57**(24), 2406–2408, DOI: **10.1016/j.jacc.2011.01.029**.

13 M. M. Richter, Electrochemiluminescence (ECL), *Chem. Rev.*, 2004, **104**(6), 3003–3036, DOI: **10.1021/cr020373d**.

14 R. J. Forster, P. Bertoncello and T. E. Keyes, Electrogenerated Chemiluminescence, *Annu. Rev. Anal. Chem.*, 2009, **2**(1), 359–385, DOI: **10.1146/annurev-anchem-060908-155305**.

15 M. A. Rezaee, M. J. Rasaee and J. Mohammadnejad, Selection of Specific Inhibitor Peptides in Enzyme-Linked Immunosorbent Assay (ELISA) of Cardiac Troponin I Using Immuno-Dominant Epitopes as Competitor, *J. Immunoassay Immunochem.*, 2017, **38**(1), 72–81, DOI: **10.1080/15321819.2016.1216444**.

16 N. Vishwakarma, S. Pandey and S. Singh, Point-of-Care Diagnostic Testing in Urgent Cardiac Care, in *Nanobiosensors for point-of-care medical diagnostics*, ed. M. Gogoi, S. Patra, D. Kundu, Springer Nature Singapore, Singapore, 2022, pp 155–171. , DOI: **10.1007/978-981-19-5141-1_7**.

17 L. Gervais, N. de Rooij and E. Delamarche, Microfluidic Chips for Point-of-Care Immunodiagnostics, *Adv. Mater.*, 2011, **23**(24), H151–H176, DOI: **10.1002/adma.201100464**.

18 G. Xing, J. Ai, N. Wang and Q. Pu, Recent Progress of Smartphone-Assisted Microfluidic Sensors for Point of Care Testing, *TrAC, Trends Anal. Chem.*, 2022, **157**, 116792, DOI: **10.1016/j.trac.2022.116792**.

19 C. Jin, Z. Wu, J. H. Molinski, J. Zhou, Y. Ren and J. X. J. Zhang, Plasmonic Nanosensors for Point-of-Care Biomarker Detection, *Mater. Today Bio.*, 2022, **14**, 100263, DOI: **10.1016/j.mtbio.2022.100263**.

20 R. Gao, F. Chen, D. Yang, L. Zheng, T. Jing, H. Jia, X. Chen, Y. Lu, S. Xu, D. Zhang and L. Yu, Simultaneous SERS-Based Immunoassay of Dual Cardiac Markers on Pump-Free Hybrid Microfluidic Chip, *Sens. Actuators B Chem.*, 2022, **369**, 132378, DOI: **10.1016/j.snb.2022.132378**.

21 Y. Liu, R. Gao, Y. Zhuo, Y. Wang, H. Jia, X. Chen, Y. Lu, D. Zhang and L. Yu, Rapid Simultaneous SERS Detection of Dual Myocardial Biomarkers on Single-Track Finger-Pump Microfluidic Chip, *Anal. Chim. Acta*, 2023, **1239**, 340673, DOI: **10.1016/j.aca.2022.340673**.

22 X. Wen, Y. Ou, H. F. Zarick, X. Zhang, A. B. Hmelo, Q. J. Victor, E. P. Paul, J. M. Slocik, R. R. Naik, L. M. Bellan, E. C. Lin and R. Bardhan, PRADA: Portable Reusable Accurate Diagnostics with Nanostar Antennas for Multiplexed Biomarker Screening, *Bioeng. Transl. Med.*, 2020, **5**(3), e10165, DOI: **10.1002/btm2.10165**.

23 A. I. Saviñon-Flores, F. Saviñon-Flores, G. Trejo, E. Méndez, Ş. Ţălu, M. A. González-Fuentes and A. Méndez-Albores, A Review of Cardiac Troponin I Detection by Surface Enhanced Raman Spectroscopy: Under the Spotlight of Point-of-Care Testing, *Front. Chem.*, 2022, **10**, 1017305, DOI: **10.3389/fchem.2022.1017305**.

24 R. Gao, Y. Mao, C. Ma, Y. Wang, H. Jia, X. Chen, Y. Lu, D. Zhang and L. Yu, SERS-Based Immunoassay of Myocardial Infarction Biomarkers on a Microfluidic Chip with Plasmonic Nanostripe Microcones, *ACS Appl. Mater. Interfaces*, 2022, **14**(50), 55414–55422, DOI: **10.1021/acsami.2c18053**.

25 M. Soroush, W. Ait Mammar, A. Wilson, H. Ghourchian, M. Salmain and S. Boujday, Design and Optimization of A Magneto-Plasmonic Sandwich Biosensor for Integration within Microfluidic Devices, *Biosensors*, 2022, **12**(10), 799, DOI: **10.3390/bios12100799**.

26 G. Huttmann and R. Birngruber, On the Possibility of High-Precision Photothermal Microeffects and the Measurement of Fast Thermal Denaturation of Proteins, *IEEE J. Sel. Top. Quantum Electron.*, 1999, **5**(4), 954–962, DOI: **10.1109/2944.796317**.

27 D. Boyer, P. Tamarat, A. Maali, B. Lounis and M. Orrit, Photothermal Imaging of Nanometer-Sized Metal Particles Among Scatterers, *Science*, 2002, **297**(5584), 1160–1163, DOI: **10.1126/science.1073765**.

28 G. Baffou, *Thermoplasmonics: Heating Metal Nanoparticles Using Light*, Cambridge University Press, Cambridge, 2017. , DOI: **10.1017/9781108289801**.

29 L. R. Hirsch, R. J. Stafford, J. A. Bankson, S. R. Sershen, B. Rivera, R. E. Price, J. D. Hazle, N. J. Halas and J. L. West, Nanoshell-Mediated near-Infrared Thermal Therapy of Tumors under Magnetic Resonance Guidance, *Proc. Natl. Acad. Sci. U. S. A.*, 2003, **100**(23), 13549–13554, DOI: **10.1073/pnas.2232479100**.

30 P. Ghosh, G. Han, M. De, C. Kim and V. Rotello, Gold Nanoparticles in Delivery Applications, *Adv. Drug Deliv. Rev.*, 2008, **60**(11), 1307–1315, DOI: **10.1016/j.addr.2008.03.016**.

31 W. Li and X. Chen, Gold Nanoparticles for Photoacoustic Imaging, *Nanomed.*, 2015, **10**(2), 299–320, DOI: **10.2217/nnm.14.169**.

32 G. Baffou, F. Cichos and R. Quidant, Applications and Challenges of Thermoplasmonics, *Nat. Mater.*, 2020, **19**(9), 946–958, DOI: **10.1038/s41563-020-0740-6**.

33 A. Campu, F. Lerouge, A.-M. Craciun, T. Murariu, I. Turcu, S. Astilean and F. Monica, Microfluidic Platform for Integrated Plasmonic Detection in Laminal Flow, *Nanotechnology*, 2020, **31**(33), 335502, DOI: **10.1088/1361-6528/ab8e72**.

34 M. Iosin, T. Scheul, C. Nizak, O. Stephan, S. Astilean and P. Baldeck, Laser Microstructuration of Three-Dimensional Enzyme Reactors in Microfluidic Channels, *Microfluid. Nanofluid.*, 2011, **10**(3), 685–690, DOI: **10.1007/s10404-010-0698-9**.

35 G. S. Bodor, S. Porter, Y. Landt and J. H. Ladenson, Development of Monoclonal Antibodies for an Assay of Cardiac Troponin-I and Preliminary Results in Suspected Cases of Myocardial Infarction, *Clin. Chem.*, 1992, **38**(11), 2203–2214.

36 A. Campu, A.-M. Craciun, M. Focsan and S. Astilean, Assessment of the Photothermal Conversion Efficiencies of Tunable Gold Bipyramids under Irradiation by Two Laser Lines in a NIR Biological Window, *Nanotechnology*, 2019, **30**(40), 405701, DOI: **10.1088/1361-6528/ab2d90**.

37 A. M. Gabudean, D. Biro and S. Astilean, Localized Surface Plasmon Resonance (LSPR) and Surface-Enhanced Raman Scattering (SERS) Studies of 4-Aminothiophenol Adsorption on Gold Nanorods, *J. Mol. Struct.*, 2011, **993**(1–3), 420–424, DOI: **10.1016/j.molstruc.2010.11.045**.

38 I. Migneault, C. Dartiguenave, M. J. Bertrand and K. C. Waldron, Glutaraldehyde: Behavior in Aqueous Solution, Reaction with Proteins, and Application to Enzyme Crosslinking, *Biotechniques*, 2004, **37**(5), 790–802, DOI: **10.2144/04375RV01**.

39 D. Maniu, V. Chis, M. Baia, F. Toderas and S. Astilean, Density Functional Theory Investigation of P-Aminothiophenol Molecules Adsorbed on Gold Nanoparticles, *J. Optoelectron. Adv. Mater.*, 2007, **9**(3), 733.

40 S. Link and M. A. El-Sayed, Shape and Size Dependence of Radiative, Non-Radiative and Photothermal Properties of Gold Nanocrystals, *Int. Rev. Phys. Chem.*, 2000, **19**(3), 409–453, DOI: **10.1080/01442350050034180**.

41 D. K. Roper, W. Ahn and M. Hoepfner, Microscale Heat Transfer Transduced by Surface Plasmon Resonant Gold Nanoparticles, *J. Phys. Chem. C*, 2007, **111**(9), 3636–3641, DOI: **10.1021/jp064341w**.

42 G. Qiu, Z. Gai, L. Saleh, J. Tang, T. Gui, G. A. Kullak-Ublick and J. Wang, Thermoplasmonic-Assisted Cyclic Cleavage Amplification for Self-Validating Plasmonic Detection of SARS-CoV-2, *ACS Nano*, 2021, **15**(4), 7536–7546, DOI: **10.1021/acsnano.1c00957**.

43 J.-P. Collet, H. Thiele, E. Barbato, O. Barthélémy, J. Bauersachs, D. L. Bhatt, P. Dendale, M. Dorobantu, T. Edvardsen and T. Folliguet, *et al.*, 2020 ESC Guidelines for the Management of Acute Coronary Syndromes in Patients Presenting without Persistent ST-Segment Elevation, *Eur. Heart J.*, 2021, **42**(14), 1289–1367, DOI: **10.1093/eurheartj/ehaa575**.

44 D. R. Lazar, F.-L. Lazar, C. Homorodean, C. Cainap, M. Focsan, S. Cainap and D. M. Olinic, High-Sensitivity Troponin: A Review on Characteristics, Assessment, and Clinical Implications, *Dis. Markers*, 2022, **2022**, 1–13, DOI: **10.1155/2022/9713326**.

45 C. M. Lombardi, V. Carubelli, A. Iorio, R. M. Inciardi, A. Bellasi, C. Canale, R. Camporotondo, F. Catagnano, L. A. Dalla Vecchia and S. Giovinazzo, *et al.*, Association of Troponin Levels With Mortality in Italian Patients Hospitalized With Coronavirus Disease 2019: Results of a Multicenter Study, *JAMA Cardiol*, 2020, **5**(11), 1274, DOI: **10.1001/jamacardio.2020.3538**.

46 N. Cantarutti, V. Battista, N. Stagnaro, M. E. Labate, M. Cicenia, M. Campisi, V. Vitali, A. Secinaro, A. Campana, G. Trocchio and F. Drago, Long-Term Cardiovascular Outcome in Children with MIS-C Linked to SARS-CoV-2 Infection—An Italian Multicenter Experience, *Biology*, 2022, **11**(10), 1474, DOI: **10.3390/biology11101474**.

47 R. Trevethan, Sensitivity, Specificity, and Predictive Values: Foundations, Pliabilities, and Pitfalls in Research and Practice, *Front. Public Health*, 2017, **5**, 307, DOI: **10.3389/fpubh.2017.00307**.

